

# Carbonic Anhydrase IX Stratifies Patient Prognosis and Identifies Nodal Status in Nasopharyngeal Carcinoma Using a Targeted Imaging Strategy

**Wenhui Huang**

Jinan University First Affiliated Hospital

**Kun Wang**

Chinese Academy of Sciences Institute of Automation

**Weiyuan Huang**

Hainan General Hospital

**Zicong He**

Jinan University First Affiliated Hospital

**Jingming Zhang**

Peking University First Hospital

**Bin Zhang**

Jinan University First Affiliated Hospital

**Zhiyuan Xiong**

The University of Melbourne

**Kelly McCabe Gillen**

Weill Cornell Medical College: Weill Cornell Medicine

**Wenzhe Li**

State Key Laboratory of Natural and Biomimetic Drugs: Peking University School of Pharmaceutical Sciences

**Feng Chen**

Hainan General Hospital

**Xing Yang**

Peking University First Hospital

**Shuixing Zhang**

Jinan University First Affiliated Hospital

**Jie Tian** (✉ [jie.tian@ia.ac.cn](mailto:jie.tian@ia.ac.cn))

Chinese Academy of Sciences Institute of Automation <https://orcid.org/0000-0003-0498-0432>

**Keywords:** carbonic anhydrase IX, nasopharyngeal carcinoma, entranodal extension, occult lymph node metastasis, ultrasonography-guided spectroscopic photoacoustic imaging

**Posted Date:** March 10th, 2022

**DOI:** <https://doi.org/10.21203/rs.3.rs-1407201/v1>

**License:**  This work is licensed under a Creative Commons Attribution 4.0 International License.

[Read Full License](#)

---

# Abstract

**Purpose:** Accurate identification of nodal status enables adequate neck irradiation for nasopharyngeal carcinoma (NPC). However, most conventional techniques are unable to pick up occult metastases, leading to underestimation of tumor extensions. Here we investigate the clinical significance of carbonic anhydrase IX (CAIX) in human NPC samples, and develop a CAIX-targeted imaging strategy to identify occult lymph node metastases (LNMs) and entrnodal extension (ENE) in animal studies.

**Methods:** 211 NPC samples are stained for CAIX and clinical outcomes are analyzed. The metastatic murine models are generated by foot pad injection of NPC cells, and a CAIX-targeted imaging agent (CAIX-800) is intravenously administered. We adopt fluorescence molecular tomography and ultrasonography (US)-guided spectroscopic photoacoustic (sPA) imaging to perform *in vivo* studies. Histological and immunohistochemical characterization are carried out via node-by-node analysis.

**Results:** For clinical samples, 90.1% (91/101) primary tumors, 73.3% (66/90) metastases and 100% (20/20) local recurrences are CAIX positive. In metastases group, 84.7% (61/72) nodal metastases and 22.2% (4/18) organ metastases are CAIX positive. CAIX expression in primary tumors is significantly associated with NPC stage and prognosis. For animal studies, CAIX-800 based fluorescence imaging achieves 81.3% sensitivity and 93.8% specificity in detecting occult LNMs *in vivo*, with a minimum detectable diameter of 1.7 mm. Coupled with CAIX-800, US-guided sPA imaging could not only detect subcapsular deposits of metastatic cancer cells two weeks earlier than conventional techniques, but also successfully track pathological ENE.

**Conclusion:** CAIX remarkably expresses in human NPCs and stratifies patient prognosis. In preclinical studies, the CAIX-800 based imaging strategy successfully identifies occult LNMs and tracks early stage of pathological ENE. This attractive method shows great translational potential, allowing medical workers to longitudinally monitor nodal status and helping to reduce unnecessary nodal biopsy for NPC patients.

## Introduction

Nasopharyngeal carcinoma (NPC), a malignancy endemic in Southeast Asia, usually infiltrate early into the local lymph basin before metastasizing through the blood [1]. In clinical practice, stage II and III NPC account for 85% patients at initial diagnosis, in which there is localized advancement and nodal involvement, but no evidence of distant metastases [2]. Unfortunately, 20–30% of these patients might develop distant metastases after a basic treatment of chemo-radiotherapy, decreasing the 5-year survival rate by 50% [3]. Several authoritative studies demonstrated that cancer cells in tumor-draining lymph nodes (LNs) obtain higher capacity to survive in human immunology system, than cells in tumor-draining blood, becoming the source of distant metastases [4, 5]. Additionally, the risk of developing distant metastases is in parallel with the increasing number of cancer-involved nodes [6]. Thus, nodal status plays a critical role in prognostication and determination of survival for NPC patients.

Currently, it remains a challenge to accurately identify nodal status on diagnostic imaging modalities for NPC. As a result, elective nodal irradiation usually covers as much potential regions of occult lymph node metastases (LNMs) as possible [7]. Moreover, adjuvant treatment escalation is commonly indicated if extranodal extension (ENE) is unexpectedly discovered [6]. Both strategies are necessary but associated with increased treatment-related toxicities and health care costs. There is a need to develop better methods for detecting the two crucial stages in lymphatic metastasis, occult LNMs and pathological ENE, under the pretreatment setting to guide NPC staging for more appropriate management. Clinically, combining several imaging modalities, such as magnetic resonance imaging (MRI), ultrasound and  $^{18}\text{F}$ -fluorodeoxyglucose positron emission tomography/computed tomography ( $^{18}\text{F}$ -FDG PET/CT) can improve the accuracy for nodal staging [7]. However, their performances remain unsatisfactory in identifying occult LNMs and pathological ENE [8], possibly due to the lack of reliable tumor biomarkers and insufficient image resolution [9, 10]. The proportion of patients with head and neck cancer diagnosed with false-negative LNs is high and ranges from 18–30% [11–13]. Even worse, radiological methods for detecting ENE are broadly subjective and unreliable, with high inter-observer variability [14, 15]. Therefore, a tumor-specific agent coupled with a novel imaging technique is desirable to accurately confirm nodal status for NPC patients.

Tumor hypoxia is a widely recognized feature of NPC, and is associated with enhanced tumor invasiveness, metastasis and radioresistance [16]. Clinically, evaluation of hypoxia is shifting to monitoring endogenous markers, especially transcriptional targets of hypoxia-inducible factors (HIFs) [17]. Carbonic anhydrase IX (CAIX) is a well-established HIFs target, and reflects persistent tumor hypoxia [17]. It is a protein that is located on the cell membrane, with a very restricted expression in the normal stomach and gut epithelial cells but a strong upregulation in many different types of tumor tissue [18]. Gene expression profiling from patient tissue samples showed that CAIX was broadly expressed in breast cancer and LNMs, but absent in peritumoral tissue and normal LNs [19]. Furthermore, high expression of CAIX in localized NPC was associated with metastatic capacity and poor prognosis, thus revealing its potential as a surrogate imaging biomarker [20, 21]. Previously, we described a fluorescently-labeled, CAIX-targeted contrast agent (CAIX-800) that could specifically visualize NPC in orthotopic xenografts [22]. To further explore its clinical potential, here we investigated the frequency and prognostic value of CAIX expression in human NPC specimens, and evaluated CAIX-800 based imaging strategy for its performance in identifying occult LNMs and pathological ENE using metastatic murine models of NPC.

We adopted fluorescence molecular tomography (FMT) and ultrasonography (US)-guided spectroscopic photoacoustic (sPA) imaging to perform *in vivo* studies. FMT provides hybrid optical and micro-CT images to visualize probe distribution in whole body at macroscopic level. US-guided sPA imaging combining the high contrast and sensitivity of optical imaging with the excellent depth resolution of US, enables to depict probe distribution in tumor-draining LNs at microscopic level. Several preclinical studies and clinical trials have demonstrated the capability of sPA imaging in detecting LNMs [23–25], and even micro-metastases as small as 50  $\mu\text{m}$  were detected [24]. These advancements led to our current innovation of applying sPA technology in identifying pathological ENE.

We aimed to characterize the clinical significance of CAIX expression in human NPC, and to subsequently establish a CAIX-targeted imaging strategy for preclinical studies (Graphical Abstract). This strategy contained two steps to address two issues. First, FMT was utilized to detect clinically undetectable nodal metastases, with sizes less than 5 mm. The diagnostic indexes were analyzed, including the diagnostic accuracy, sensitivity, specificity, positive predictor value (PPV), and negative predictor value (NPV). Second, US guided sPA imaging was explored for its potential role in identifying and tracking pathological ENE.

## **Material And Methods**

### **Human subjects**

We retrospectively analyzed the demographic information of 211 patients with pathologically proven NPC (Table S.1). The median cohort age was 58 years old and 132 (62.5%) patients were male. Patients underwent pretreatment evaluation, including physical examination, hematology and biochemistry profiling, fiber optic nasopharyngoscopy, MRI, chest radiography, abdominal US, and/or PEC/CT. Clinical staging was done according to the American Joint Committee on Cancer (AJCC) 8th edition tumor-node-metastasis (TNM) staging systems [6]. None of the patients had received treatment before biopsy collection. Radiation alone was the standard treatment for stage I NPC, and concurrent chemoradiotherapy with or without induction/adjuvant chemotherapy was recommended for stages II to IVB disease according to the NCCN guidelines for head and neck tumors [26]. Due to the absence of stage I in our study, all patients received chemotherapy plus radiation therapy.

### **Cell culture**

Human NPC lines including SUNE1, 5-8F, 6-10b, S18, C666-1, CNE1, CNE2, and HONE1 cell lines were obtained from Sun Yat-sen University Cancer Center. All NPC cell lines used in this study were authenticated using short tandem repeat profiling. Cultures were maintained in 37°C with 5% CO<sub>2</sub>. Cells were split using 0.25% Trypsin-EDTA (Gibco, CA). All cell lines were cultured in Dulbecco's Modified Eagle's Medium (Gibco, CA) supplemented with 10% fetal bovine serum (Gibco, CA), 100 units/ml penicillin, 100 ug/ml streptomycin, and 1% L-glutamine. All cell lines were tested mycoplasma-free every 3 weeks.

### **Western blot**

Cells were trypsinized, pelleted, washed three times with ice cold PBS, and lysed in RIPA buffer. Protein concentrations were determined using the BCA assay (ThermoFisher, US). In brief, 20 µg of total protein per sample was loaded into each lane of a NuPAGE 4–12% Bis-Tris protein gels for electrophoresis at 100 V for 100 min. Wet transfer was performed using a Bio-Rad transfer kit at 250 mA for 60 min. The transferred nitrocellulose membrane was blocked in PBS containing 5% BSA and 0.1% Tween-20 for 1.5 h. Rabbit anti-human CAIX mAb (1:1000, ab184006) was incubated in the blocking buffer overnight at 4°C. The membrane was washed with PBS containing 0.1% Tween-20, and then, secondary antibody incubation (1:10000, ab6721) was performed in the blocking buffer for 2 h at room temperature. After

washing four times with PBS containing 0.1% Tween-20, membranes were analyzed in an Odyssey Infrared imaging system (LI-COR Biosciences, NE, USA).

## **CAIX-800 and targeting efficiency *in vitro***

The synthesis of CAIX ligand was performed by Shanghai Apeptide Co.,Ltd. (China), and conjugation with IRDye® 800CW infrared dyes (LI-COR Biosciences, USA) was reported in our previous study [22]. High performance liquid chromatography (Shimadzu, Milan, Italy) and mass spectroscopy (Santa Clara, CA) was applied to confirm the optical agent, CAIX-800. To validate the targeting specificity, two cell lines (5-8F and S18) with high level of CAIX expression were co-incubated with CAIX-800 for half an hour, then fixed and imaged via Andor Dragonfly High Speed Confocal Platform (Dragonfly 500, Oxford Instruments, England). The blocking group, using CAIX ligand without dye conjugation to pretreat cells for 30 minutes before adding CAIX-800, was tested as control.

## **Animal subjects**

The animals used in our study were four-week-old male BALB/c nude mice, purchased from Vital River Laboratory Animal Technology Co. Ltd. (Beijing, China). The metastatic murine models were generated by foot pad injection of 5-8F cells ( $1.2 \times 10^6$  in 30  $\mu$ l DPBS) or S18 cells ( $4.5 \times 10^5$  in 30  $\mu$ l DPBS).

## **FMT and data analysis**

Fluorescence imaging was performed at pre, 3h, 9h, 12h, 24h, 48h time points via the IVIS spectrum CT system (PerkinElmer, Waltham, MA). For 2D epi-fluorescence imaging, eight pairs of excitation and emission filters (ex/em: 675/720; 675/740; 675/760; 710/760; 675/780; 710/780; 710/800; 710/820) were used for spectral unmixing. For 3D FMT, a CT dataset was acquired to establish the animal's surface boundary for tomography reconstruction. Then, a series of fluorescent surface radiance images were acquired at multiple trans-illumination locations encompassing the region of interest (ROI). The ROI covered kidneys and regional nodes, including popliteal lymph nodes (PLNs), sciatic lymph nodes (SLNs), inguinal lymph nodes (ILNs), and lumbar lymph nodes (LLNs). The primary tumor was excluded in ROI, since the recommended scan fields should perfectly match the target to ensure the most accurate and repeatable results. For data analysis, imaging data were calculated as mean fluorescent intensity (MFI) using spectral unmixing to avoid multiple interfering fluorescent signal. Immediately after nodal resection, regional nodes were re-scanned using the same 2D imaging protocol, and then compared to histopathology.

## **US-guided sPA imaging**

Photoacoustic signal was obtained on a Vevo LAZR-X imaging system (VisualSonics, Japan) with a 21 MHz (15–30 MHz) linear array transducer (MX 250, axial resolution: 75  $\mu$ m). Images were acquired at different time points (0h, 2h, 8h, 24h). In order to differentiate cancer cells labeled with CAIX-800 from the background, we implemented spectroscopic analysis to resolve the hemoglobin and CAIX-800, which are two major contributors of PA signal in the near-infrared wavelength region. The PLNs were imaged at multiple wavelengths (680 nm, 695 nm, 740 nm, 800 nm, 860 nm) for accurate spectral classification. For

3D image acquisition, the transducer was automatically scanned by a stepping motor with a step size of 0.5 mm. Spectroscopic imaging thresholds (range 0-100) were maintained at the following values: brightness to 45, opacity to 99, contrast to 90 and threshold to 90. The Vevo LAB 3.2.6 software (VisualSonics, Japan) was utilized for data analysis. ROIs were drawn in every five consecutive cross-sections in each lymph node on US, and nodal volumes were automatically obtained.

## **Pathological and histochemical analysis**

In human study, paraffin-embedded tissue from biopsy samples were sectioned at 4  $\mu\text{m}$  and mounted on lysine coated glass slides. All sections from patients were stained with hematoxylin and eosin (H&E), and an anti-CAIX antibody (1:250, abcam184006, USA). Histological characterization and immunohistochemistry scoring were performed by two head and neck pathologists, who were unaware of each other's scores and blinded to clinical information from each patient. Semi-quantitative assessment of CAIX staining was scored considering both staining intensity and the extent of staining. Staining intensity was based on a 4-point scale from 0 to 3 (0, negative; 1, weak; 2, moderate; 3, strong). The extent of staining was recorded as a percentage of cancer cells that were CAIX positive. Each section was scored by multiplying the intensity score with the positive area. A score of zero indicated no evidence of specific immunostaining. Slides were digitally scanned at 20x magnification into whole-slide digital images using a digital slide scanner (Pannoramic® MIDI II, 3DHISTECH Ltd., Hungary). Whole-slide images were viewed by CaseViewer 2.4 (3DHISTECH Ltd., Hungary).

In animal studies, to quantify probe distribution and antibody uptake on microscopic images, the resected nodes were flash frozen at  $-80^{\circ}\text{C}$  in a deep freeze, and then serial frozen sections were cut. For CAIX-800 distribution, 10  $\mu\text{m}$  thick sections were scanned using an Andor Dragonfly High Speed Confocal Platform (Dragonfly 500, Oxford Instruments, England), with an excitation of 730 nm and an emission of 809 nm. Corresponding 4  $\mu\text{m}$  thick sections were stained with H&E. Slides were reviewed by the two pathologists mentioned above, who outlined tumor boundaries to identify cancerous regions.

## **Statistics**

GraphPad Prism (9.0.0, GraphPad Software, San Diego, CA) was used for statistical analysis. For correlations, linear least squares fitting was performed at the 95% confidence level, and the Pearson correlation coefficient was used to quantify correlations between different variables. Comparative analysis was performed using a student's t-test, chi-square test or Fisher's exact test. Binary differences were calculated using odds ratio (OR). Receiver operating characteristic curve (ROC) was constructed to describe the diagnostic accuracy for malignant nodes detection and subtyping. Cutoff points were selected using Youden's index, which maximized the sum of sensitivity and specificity. X-tile (Version 3.4.7) was utilized to obtain the optimal threshold value for the Kaplan-Meier estimates. All tests were two sided, and p values  $< 0.05$  was considered statistically significant.

## **Results**

# CAIX expression in tumor specimens positively associated with tumor stage

We quantified CAIX expression in human NPC specimens (n = 211, Fig. 1.A). Three groups, primary tumors (n = 101), metastases (n = 90) and local recurrences (n = 20), were analyzed. In metastases group, 72 (80%) were nodal metastases, and 18 (20%) were organ metastases including metastases in lung (n = 11), liver (n = 4) and bone (n = 3). We found an increase in CAIX expression within tumors as compared to nasal mucosa (n = 10, Figure S.1). In the primary tumors group, correlations between CAIX expression and clinical information (including T stage, N stage, M stage, tumor stage, pathological type, gender, and age) were analyzed (Fig. 1.B). We found that there were significantly positive correlations between CAIX expression and T stage ( $r = 0.3546$ ,  $p = 0.0003$ ), M stage ( $r = 0.2190$ ,  $p = 0.0278$ ) and tumor stage ( $r = 0.2415$ ,  $p = 0.0150$ ).

Remarkably, 90.1% (91/101) primary tumors, 73.3% (66/90) metastases and 100% (20/20) local recurrences were CAIX positive (Table 1, Fig. 1.C). There was no significant difference in CAIX scores between primary and locally recurrent tumors ( $p = 0.223$ ), but a marked significance between primary and metastatic tumors ( $p < 0.0001$ ). Compared with the metastatic tumors, primary and locally recurrent tumors had higher level of CAIX scores (primary tumors,  $1.0 \pm 0.62$ ; local recurrences,  $1.2 \pm 0.74$ ; metastases,  $0.5 \pm 0.49$ ).

In metastases group, 84.7% (61/72) nodal metastases were CAIX positive. 77.8% (14/18) organ metastases were CAIX negative, and 56% (14/25) CAIX-negative samples were from organ metastases. These results suggest that CAIX might be a suitable biomarker for primary NPC, local recurrences, and nodal metastases, but not organ metastases.

## High CAIX expression in primary tumors correlated with poor outcome

CAIX expression in primary NPC was positively correlated with prognostic outcome [20], and thus imaging CAIX for NPC patients at initial diagnosis might provide valuable prognostic information. To explore its prognostic value in our study, Kaplan-Meier survival curves for progression free survival (PFS) were performed and displayed in Fig. 1.D. X-tile was used to obtain the optimal cutoff point of 1.16. Based on the cutoff point, we classified CAIX score as low ( $< 1.16$ , n = 55) and high ( $\geq 1.6$ , n = 46) groups. The median PFS was 696.7 days. A statistically significant worse outcome ( $p < 0.001$ ) was noted in high CAIX group, compared to low CAIX group. CAIX status was a significant risk factor for disease progression, with a risk ratio of 4.441 (95% CI: 2.217–9.308) using Fisher's exact test (Fig. 1.E). Together, these findings suggested that quantified CAIX expression would help to guide NPC staging and predict prognostic outcome.

## *In vitro* study confirmed CAIX-800 targeting efficiency

To explore CAIX expression in human NPC cell lines, we screened the levels of CAIX in a serial of cell lines, including SUNE1, 5-8F, 6-10b, S18, C666-1, CNE1, CNE2, and HONE1 cell lines. All cell lines expressed CAIX protein, but at different levels (Figure S.2). 5-8F and S18 had the highest CAIX expression, which might associate with their strong capacity for metastasis [27]. Thus, it is feasible to use CAIX as a target for their tumor xenografts.

A fluorescently labeled small-molecule inhibitor of CAIX, CAIX-800, was used for subsequent imaging studies [22]. The probe contained two parts, a dual-motif ligand that offered excellent binding affinity to the CAIX receptor [28, 29], and a near infrared dye IRDye 800 CW that is well-known for its predominantly optical and photoacoustic properties [25] (Figure S.3). Confocal microscopy images revealed that CAIX-800 showed specific accumulation in the 5-8F and S18 cell lines, and presented off-target effect in blocking groups, suggesting its efficient targeting capability for CAIX receptor (Figure S.4).

## Fluorescence molecular imaging identified occult LNMs

To study the feasibility of CAIX-800 in localizing to occult LNMs, we implanted 5-8F cells in the foot pads of nude mice and allowed them to metastasize to the draining LNs (Fig. 2.A). Twenty-one days after the primary tumor implantation, 200  $\mu$ L of CAIX-800 (15  $\mu$ M) was intravenously injected into each mouse. The analysis of 2D fluorescent images across different time points (pre, 3, 6, 9, 12, 24, and 48 hours) revealed that images at 24-hour had the highest contrast, probably because CAIX-800 had been cleaned up from the blood pool. Fluorescent signal from CAIX-800 showed selective retention in foot pad tumors, tumor-draining LNs and the metabolic organs (kidneys and bladder). The optical and micro-CT hybrid images clearly visualized regional LNs (Fig. 2.B). 24 hours post injection, a total of 13 mice received euthanasia and their bilateral nodes ( $n = 57$ ) were resected to perform histological examinations. All nodes were less than 5 mm in diameter, which is under the detection threshold of physical examination and conventional techniques. The mapping LNs showed significantly higher signal than the opposite region of LNs both *in vivo* and *ex vivo* (Fig. 2.C). *Ex vivo* quantification of MFI in organs and foot pad tumors after sacrificing mice also confirmed the good selectivity of CAIX-800 (Figure S.5).

Metastatic NPCs usually follow a predictable pattern of lymphatic metastases, with low risk of skip metastasis [30]. Thus, cancer cells firstly drain to the nearest LNs known as the sentinel nodes, then transport to the second, or the third station of nodes following lymphatic drainage. We analyzed optical signal from different regions of LNs, and found that the regions nearer to the primary tumor had a higher number of positive LNs (Fig. 2.D-E). That is in consistent with the lymphatic spread pattern. Thus, CAIX-800 could identify not only the sentinel LNs, but also distant regions of occult metastases, with the detection threshold reaching 1.7 mm.

The MFI of malignant LNs was significantly higher than that of benign LNs both *in vivo* ( $7.1 \pm 2.1$  vs.  $4.0 \pm 1.4$ ,  $p < 0.0001$ ) and *ex vivo* ( $5.1 \pm 2.2$  vs.  $1.7 \pm 0.8$ ,  $p < 0.0001$ , Fig. 2.F). The ROCs based on MFI (Fig. 2.G) demonstrated that using CAIX-800 based fluorescent imaging achieved 81.3% sensitivity and 93.8% specificity *in vivo* (threshold MFI = 5.825), as well as 87.5% sensitivity and 93.8% specificity *ex vivo* (threshold MFI = 2.860), in detecting occult LNMs (Table 2). The area under the curve (AUC) obtained for

MFI was 0.898 *in vivo*, and 0.949 *ex vivo*. The PPVs were 92.8% *in vivo* and 93.3% *ex vivo*; the NPVs were 83.3% *in vivo* and 88.2% *ex vivo*.

The above experiments were repeated and validated in mice with S18 foot pad xenografts. A total of 14 mice received euthanasia, and their bilateral nodes (n = 71) were resected for fluorescent imaging and histological examinations. Of all LNs, 39 had histologically detected metastases. We applied the same threshold value as before (MFI = 2.860) for distinguishing between benign and malignant nodes *ex vivo*. Then, the diagnostic accuracy reached 0.9, with 90.6% specificity and 89.7% sensitivity. The PPV and NPV were 92.1% (35/38) and 87.9% (29/33), respectively.

To further evaluate CAIX-800 distribution in LNs, we compared the fluorescent slices to H&E staining within malignant LNs (true positive, false negative) and benign LNs (true negative, false positive), shown in Fig. 3. In malignant LNs, the signal from CAIX-800 was mostly found in the metastatic foci, demonstrating consistency with the distribution of tumor cells as indicated by H&E staining. Interestingly, in the false negative LNs (4/33), CAIX-800 was not absent, but only accumulated along the edge of necrotic core inside the tumor nest, which was insufficient to generate detectable signal. Based on our findings in human specimens from local recurrences, such perinecrotic area was highly hypoxic (Figure S.6), which explained the targeting behavior of CAIX-800. There were three false positive LNs (3/38) with rich drainage vein and lymph vessels, depicting moderate signal uniformly distributing in the whole slices. This suggested that probably through non-selectively perfusion into regional LNs during passive lymphatic flow, CAIX-800 showed selective retention in the tumor area within tumor-draining LNs.

## US-guided sPA imaging identified pathological ENE

ENE refers to the growth of cancer cells in lymph nodes beyond the confine of nodal capsule (Fig. 4.A). To test the utility of sPA imaging in detecting ENE, 200  $\mu$ L of CAIX-800 (25  $\mu$ M) was intravenously injected into each mouse at the 5th week of bearing 5-8F tumors (n = 6), when the volume of tumor draining PLNs rose to 60–80 mm<sup>3</sup>. Normal lymph nodes were identifiable by a dark bean-shaped region on the grayscale ultrasound, when the transducer was applied to the popliteal fossa and scanned in the transverse section (yellow dashed circles, Fig. 4.B). Overlaid US and sPA images taken 2 hours post-injection depicted CAIX-800 accumulation in the thickened tumor-draining lymphatic vessel and the subcapsular sinus of PLN, while there was only a sporadic signal in the opposite region of PLN (O-PLN). Twenty-four hours post injection, US and sPA overlaid 3D images visualized the CAIX-800 distribution in peri-nodal space around some metastatic LNs (3/6) (Fig. 4.C, Video.1), which was consistent with the optical features of ENE reported in a recent study [31]. Quantitative analysis showed a strong increase of sPA signal in tumor-filled PLNs across time points, but no apparent change in the O-PLNs (Fig. 4.D). In immunological staining from the *ex vivo* specimens, tumor cells presented a prominent nesting pattern, and expressed high level of CAIX while infiltrating into the nodal capsule with overlying capsule thickening, which correlated with *in vivo* findings (Fig. 4.E).

To further monitor nodal status, a cohort of mice bearing 5–8F foot pad tumors (n = 15) were intravenously injected with CAIX-800 and imaged weekly to follow changes in PLNs. The schematic

timeline for imaging and histological analysis was shown in Figure S.7. MRI, US, and high frequency US-guided sPA showed significant changes in the PLNs (Fig. 5.A). With the increase of nodal volumes, the axial T2WI and the US demonstrated significantly enlarged LNs four weeks after bearing foot pad tumors ( $p < 0.01$ ) (Fig. 5.B). At this time point, bean-shaped LNs became distinctly swollen, and the isointense within swollen LNs changed to the hyperintense on axial T2WI. Moreover, the echogenic hilum vanished on ultrasonic images. All those evidences on MRI and US indicated the presence of metastases at the 4th week according to the clinical practice [32]. However, the significant increase of sPA signal ( $p < 0.01$ ) implied that metastases were already presented at the 3rd week, prior to changes in the nodal volume (Fig. 5.C). These results demonstrated US-guided sPA imaging coupled with CAIX-800 was more sensitive to identify nodal status than conventional imaging techniques.

After node-by-node analysis, two important findings indicated US-guided sPA imaging had optimal imaging resolution for detecting both micro-metastatic deposits and pathological ENE. Firstly, two nodes (2/12) at the 2nd week were found abundant sPA signal locally distributing in the subcapsular sinus, and the corresponding histology confirmed micro-metastases without ENE, demonstrating this technique could detect occult LNMs two weeks earlier than conventional imaging. Secondly, 1/9 nodes at the 3rd week, 3/6 nodes at the 4th week, and 1/3 nodes at the 5th week showed the distinct signal localizing to nodal periphery at 24h post injection, suggesting that tumor cells might break through the capsule into peripheral tissue. The presence of ENE was finally validated by H&E staining (the last row, Fig. 5.A). Notably, the sPA signal distinctly decreased at the 5th week with the enlarging nodal size. It was definitely consistent with rim enhancement on contrast-enhanced CT/MRI, which might be associated with the solid stress from rapidly proliferating tumor collapsing lymphatic vessels [33]. On displayed fluorescence slice (Fig. 5.D), CAIX-800 was found not only distributing within the tumor foci, but also in tumor infiltrated capsule, when it was peeled off *ex vivo*. Taken together, these results further validated the good performance of US-guided sPA coupled with CAIX-800 in identifying and tracking pathological ENE.

## Discussion

We demonstrated that hypoxia-induced CAIX remarkably expressed in human NPCs and stratified patient prognosis. These findings encouraged us to develop a CAIX-targeted imaging strategy. In metastatic murine models of NPC, CAIX-800 based fluorescence imaging had superior performance in detecting occult LNMs, with a minimum detectable diameter of 1.7 mm. Coupled with CAIX-800, US-guided sPA not only achieved effective detection of early micro-metastases within LNs, but also captured pathological ENE, which would give a critical feedback for better treatment in clinical practice.

Our clinical cohort experience might have two clinical advantages. First, tumor hypoxia is a well-known hallmark of radiation resistance in head and neck cancers, yet imaging hypoxia has proven to be very challenging [34, 35]. High expression of CAIX in primary lesions is associated with chronic hypoxia, leading to hypoxia-induced radioresistance and poor prognosis. Using a CAIX-specific contrast agent in NPC diagnostic imaging would help evaluate tumor hypoxia and provide additional prognostic information. Second, CAIX expression was prevalent in locally recurrent tumors, supporting the potential

of imaging CAIX to identify locally recurrent NPC, which has been a challenge in clinical practice, due to the coexistence of the highly variable appearance of recurrent tumors and complex changes in post-chemoradiation tissue [36]. The inconsistency of CAIX expression between nodal metastases and organ metastases might be due to the distinct function of tumor hypoxia in organ-specific metastasis [37], which is worthy of testing in a larger cohort.

Even in the age of molecular medicine, nodal status remains the strongest predictor of prognosis [38]. Recently, it was shown that metastatic tumor cells in nodes preferentially use fatty acids rather than glucose as a fuel source [39], indicating that  $^{18}\text{F}$ -FDG PET imaging, the most commonly used technique in detecting metastases by measuring glucose high-uptake, might be unsuitable for identifying nodal metastases. Another issue for PET imaging was its limited sensitivity in detecting metastatic deposits and inability to reliably detect metastases less than  $80\text{ mm}^3$  [40, 41]. Here our study demonstrated the feasibility of detecting small metastases (diameter less than 5 mm, volume range from  $3\text{ mm}^3$  to  $15\text{ mm}^3$ ) using CAIX-800 based fluorescence imaging, with sensitivity of 81.3%, specificity of 93.8%, PPV of 92.8% and NPV of 83.3% *in vivo*. Even very small nodes, with a minimum detectable diameter of 1.7 mm, were identified within normal-sized LNs. Such microscopic tumor deposits are below the threshold of detection using conventional imaging techniques. These results provided a first step towards exploring the potential of CAIX-800 as a fluorescence imaging agent for NPC patients in near-infrared fluorescence-guide surgery, since salvage surgery has been recommended for NPC patients with locoregional recurrence or persistent disease to improve survival outcome [42, 43].

Another important finding was that the US-guided sPA technology could be used to identify pathological ENE. Beyond occult LNMs in patients with radiologically node-negative necks, a higher nodal category of ENE may necessitate unplanned adjuvant therapies [44]. A previous meta-analysis based on 3391 nodes from head and neck tumors showed a sensitivity of 76% and specificity of 77% for CT, a sensitivity of 72% and specificity of 78% for MRI, and a sensitivity of 80% and specificity of 83% for PET when predicting ENE [14]. Thus, attempts to reliably identify ENE using conventional methods have been less successful. The sPA system integrates high temporal and spatial resolution, deep penetration, and multiplex contrasts. These advantages help to push forward the translation from pre-clinical science to the clinical setting [23, 31]. Taking advantage of a non-invasive, non-radioactive and fast imaging technique, it is also suitable for long-term monitoring. After weekly scans in our study, sPA imaging successfully identified subcapsular deposits of cancer cells and surprisingly captured pathological ENE at 24h intravenous injection of CAIX-800. To our best of knowledge, it is the first report of imaging hypoxic marker to track early stage of ENE. This technique exceeds the sensitivity limitation of conventional imaging methods for detecting ENE, allowing medical workers to longitudinally identify nodal status and helping to decrease unnecessary radiation exposure for NPC patients.

There are also some limitations in this study. First, regarding the human data, each tumor specimen was obtained from a single patient, since it was quite difficult to obtain primary, metastatic and recurrent tissue from the same patient. Second, the recorded tumor stage was clinical stage based on clinical examination and radiological assessment, rather than pathological stage. Thus, the analysis of the

correlation might be underpowered. Third, regarding the animal study, although microscopic imaging of CAIX-800 strongly corresponded with metastatic deposits within LNs that showed CAIX expression, there were still false-negative nodes (4/32), depicting CAIX-800 just predominantly accumulated at the periphery of the metastases, which is consistent with the results of several clinical trials using tumor specific imaging tracers for discrimination of malignant and benign LNs [11, 45]. Fourth, we successfully observed pathological ENE via US guided sPA imaging, but an analysis of diagnostic performance was absent due to the small size of database. Future investigations using a larger cohort of metastatic NPC models or clinical trails are needed.

In conclusion, we demonstrated that high CAIX expression in human NPC specimens was associated with advanced stage and poor prognosis, which uncovered the potential of imaging CAIX to guide staging and risk stratification for NPC patients. In animal studies, CAIX-800 based imaging strategies showed sensitive and specific in detecting occult LNMs, and successfully identified early stage of pathological ENE. We believe these findings may finally benefit image-guided radiotherapy or surgery for NPC patients in the near future.

## **Declarations**

### **Funding**

We acknowledge financial support from the Ministry of Science and Technology of China (Grant Nos. 2017YFA0205200), the National Natural Science Foundation of China (Grants Nos. 82027803, 62027901, 81930053, 81227901, 81871346, 81871323), the Chinese Academy of Sciences (Grants Nos. YJKYYQ20180048 and QYZDJ-SSW-JSC005), the Excellent Member Project of Youth Innovation Promotion Association CAS, and the Project of High-Level Talents Team Introduction in Zhuhai City, the instrumental and technical support of Multimodal Biomedical Imaging Experimental Platform, Institute of Automation, Chinese Academy of Sciences.

### **Competing Interests**

The authors have no relevant financial or non-financial interests to disclose.

### **Author Contributions**

All authors contributed to the study conception and design.

Material preparation, data collection and analysis: Wenhui Huang, Kun Wang, Weiyuan Huang, Feng Chen, Zicong He,

Jingming Zhang, Bin Zhang, Zhiyuan Xiong, Wenzhe Li.

Writing the first draft: Wenhui Huang, Kun Wang, Weiyuan Huang.

Revising the manuscript: Jie Tian, Shuixing Zhang, Xing Yang, Kelly McCabe Gillen.

All authors read and approved the final manuscript.

## Data Availability

The datasets generated during and/or analysed during the current study are available from the corresponding author on reasonable request.

## Ethics approval

In human subjects, the study was approved by the Institutional Review Board at the Hainan General Hospital (Permit Number: 2018-0928-26). In animal subjects, all experiments were performed according to the guidelines of the Institutional Animal Care and Use Committee of Beijing Municipal Science & Technology Commission (Permit Number: 2020-0049).

## Consent to participate

Written informed consent was obtained from the patients before starting the study.

## References

1. Chen YP, Chan ATC, Le QT, Blanchard P, Sun Y, Ma J. Nasopharyngeal carcinoma. *Lancet*. 2019;394:64–80.
2. Tang XR, Li YQ, Liang SB, Jiang W, Liu F, Ge WX, et al. Development and validation of a gene expression-based signature to predict distant metastasis in locoregionally advanced nasopharyngeal carcinoma: a retrospective, multicentre, cohort study. *Lancet Oncol*. 2018;19:382–93.
3. Wong KCW, Hui EP, Lo KW, Lam WKJ, Johnson D, Li L, et al. Nasopharyngeal carcinoma: an evolving paradigm. *Nat Rev Clin Oncol*. 2021;18:679–95.
4. Pereira ER, Kedrin D, Seano G, Gautier O, Meijer EFJ, Jones D, et al. Lymph node metastases can invade local blood vessels, exit the node, and colonize distant organs in mice. *Science*. 2018;359:1403–7.
5. Ubellacker JM, Tasdogan A, Ramesh V, Shen B, Mitchell EC, Martin-Sandoval MS, et al. Lymph protects metastasizing melanoma cells from ferroptosis. *Nature*. 2020;585:113–8.
6. Lydiatt WM, Patel SG, O'Sullivan B, Brandwein MS, Ridge JA, Migliacci JC, et al. Head and Neck cancers-major changes in the American Joint Committee on cancer eighth edition cancer staging manual. *CA Cancer J Clin*. 2017;67:122–37.
7. Van den Bosch S, Vogel WV, Raaijmakers CP, Dijkema T, Terhaard CHJ, Al-Mamgani A, et al. Implications of improved diagnostic imaging of small nodal metastases in head and neck cancer: Radiotherapy target volume transformation and dose de-escalation. *Radiother Oncol*. 2018;128:472–8.
8. McMullen CP, Garneau J, Weimar E, Ali S, Farinhas JM, Yu E, et al. Occult nodal disease and occult extranodal extension in patients with oropharyngeal squamous cell carcinoma undergoing primary

- transoral robotic surgery with neck dissection. *JAMA Otolaryngol Head Neck Surg.* 2019;145:701–7.
9. Bhattacharya P, Mukherjee R. Lymph node extracapsular extension as a marker of aggressive phenotype: Classification, prognosis and associated molecular biomarkers. *Eur J Surg Oncol.* 2021;47:721–31.
  10. Alavi A, Carlin SD, Werner TJ, Al-Zaghal A. Suboptimal sensitivity and specificity of PET and other gross imaging techniques in assessing lymph node metastasis. *Mol Imaging Biol.* 2019;21:808–11.
  11. Nishio N, van den Berg NS, van Keulen S, Martin BA, Fakurnejad S, Teraphongphom N, et al. Optical molecular imaging can differentiate metastatic from benign lymph nodes in head and neck cancer. *Nat Commun.* 2019;10:5044.
  12. Civantos FJ, Zitsch RP, Schuller DE, Agrawal A, Smith RB, Nason R, et al. Sentinel lymph node biopsy accurately stages the regional lymph nodes for T1-T2 oral squamous cell carcinomas: results of a prospective multi-institutional trial. *J Clin Oncol.* 2010;28:1395–400.
  13. Pesek S, Ashikaga T, Krag LE, Krag D. The false-negative rate of sentinel node biopsy in patients with breast cancer: a meta-analysis. *World J Surg.* 2012;36:2239–51.
  14. Abdel-Halim CN, Rosenberg T, Dyrvig AK, Høilund-Carlsen PF, Sørensen JA, Rohde M, et al. Diagnostic accuracy of imaging modalities in detection of histopathological extranodal extension: A systematic review and meta-analysis. *Oral Oncol.* 2021;114:105169.
  15. Kann BH, Hicks DF, Payabvash S, Mahajan A, Du J, Gupta V, et al. Multi-institutional validation of deep learning for pretreatment identification of extranodal extension in head and neck squamous cell carcinoma. *J Clin Oncol.* 2020;38:1304–11.
  16. Rankin EB, Giaccia AJ. Hypoxic control of metastasis. *Science.* 2016;352:175–80.
  17. Wilson WR, Hay MP. Targeting hypoxia in cancer therapy. *Nat Rev Cancer.* 2011;11:393–410.
  18. Lou Y, McDonald PC, Oloumi A, Chia S, Ostlund C, Ahmadi A, et al. Targeting tumor hypoxia: suppression of breast tumor growth and metastasis by novel carbonic anhydrase IX inhibitors. *Cancer Res.* 2011;71:3364–76.
  19. Tafreshi NK, Bui MM, Bishop K, Lloyd MC, Enkemann SA, Lopez AS, et al. Non-invasive detection of breast cancer lymph node metastasis using carbonic anhydrases IX and XII targeted imaging probes. *Clin Cancer Res.* 2012;18:207–19.
  20. Koukourakis MI, Bentzen SM, Giatromanolaki A, Wilson GD, Daley FM, Saunders MI, et al. Endogenous markers of two separate hypoxia response pathways (hypoxia inducible factor 2 alpha and carbonic anhydrase 9) are associated with radiotherapy failure in head and neck cancer patients recruited in the CHART randomized trial. *J Clin Oncol.* 2006;24:727–35.
  21. Hui EP, Chan AT, Pezzella F, Turley H, To KF, Poon TC, et al. Coexpression of hypoxia-inducible factors 1alpha and 2alpha, carbonic anhydrase IX, and vascular endothelial growth factor in nasopharyngeal carcinoma and relationship to survival. *Clin Cancer Res.* 2002;8:2595–604.
  22. Huang W, Wang K, An Y, Meng H, Gao Y, Xiong ZY, et al. In vivo three-dimensional evaluation of tumour hypoxia in nasopharyngeal carcinomas using FMT-CT and MSOT. *Eur J Nucl Med Mol Imaging.* 2020;47:1027–38.

23. Yu Q, Huang SS, Wu ZY, Zheng JD, Chen XY, Nie LM. Label-free visualization of early cancer hepatic micrometastasis and intraoperative image-guided surgery by photoacoustic imaging. *J Nucl Med*. 2020;61:1079–85.
24. Luke GP, Myers JN, Emelianov SY, Sokolov KV. Sentinel lymph node biopsy revisited: ultrasound-guided photoacoustic detection of micrometastases using molecularly targeted plasmonic nanosensors. *Cancer Res*. 2014;74:5397–408.
25. Nishio N, van den Berg NS, Martin BA, van Keulen S, Fakurnejad S, Rosenthal EL, et al. Photoacoustic molecular imaging for the identification of lymph node metastasis in head and neck cancer using an anti-EGFR antibody-dye conjugate. *J Nucl Med*. 2021;62:648–55.
26. Colevas AD, Yom SS, Pfister DG, Spencer S, Adelstein D, Adkins D, et al. NCCN guidelines insights: head and neck cancers, version 1. 2018. *J Natl Compr Canc Netw*. 2018;16:479–90.
27. Zong D, Yin L, Zhong Q, Guo WJ, Xu JH, Jiang N, et al. ZNF488 enhances the invasion and tumorigenesis in nasopharyngeal carcinoma via the wnt signaling pathway involving epithelial mesenchymal transition. *Cancer Res Treat*. 2016;48:334–44.
28. Wichert M, Krall N, Decurtins W, Franzini RM, Pretto F, Schneider P, et al. Dual-display of small molecules enables the discovery of ligand pairs and facilitates affinity maturation. *Nat chem*. 2015;7:241–9.
29. Yang X, Minn I, Rowe SP, Banerjee SR, Gorin MA, Brummet M, et al. *Imaging of carbonic anhydrase IX with an <sup>111</sup>In-labeled dual-motif inhibitor*. *Oncotarget*. 2015;6:33733–42.
30. Ho FC, Tham IW, Earnest A, Lee KM, Lu JJ. Patterns of regional lymph node metastasis of nasopharyngeal carcinoma: a meta-analysis of clinical evidence. *BMC Cancer*. 2012;12:98.
31. Krishnan G, van den Berg NS, Nishio N, Juniper G, Pei J, Zhou Q, et al. Metastatic and sentinel lymph node mapping using intravenously delivered Panitumumab-IRDye800CW. *Theranostics*. 2021;11:7188–98.
32. Morawitz J, Bruckmann NM, Dietzel F, Ullrich T, Bittner AK, Hoffmann O, et al. *Determining the axillary nodal status with four current imaging modalities including <sup>18</sup>F-FDG PET/MRI in newly diagnosed breast cancer: A comparative study using histopathology as reference standard*. *J Nucl Med*. 2021;62:1677–83.
33. Jones D, Wang Z, Chen IX, Zhang S, Banerji R, Lei PJ, et al. Solid stress impairs lymphocyte infiltration into lymph-node metastases. *Nat Biomed Eng*. 2021;5:1426–36.
34. Horsman MR, Mortensen LS, Petersen JB, Busk M, Overgaard J. Imaging hypoxia to improve radiotherapy outcome. *Nat Rev Clin Oncol*. 2012;9:674–87.
35. Liu JN, Bu W, Shi J. Chemical design and synthesis of functionalized probes for imaging and treating tumour hypoxia. *Chem Rev*. 2017;117:6160–224.
36. Zhou H, Shen G, Zhang W, Cai H, Zhou Y, Li L. *<sup>18</sup>F-FDG PET/CT for the diagnosis of residual or recurrent nasopharyngeal carcinoma after radiotherapy: a meta-analysis*. *J Nucl Med*. 2016;57:342–7.

37. Lu X, Yan CH, Yuan M, Wei Y, Hu G, Kang Y. In vivo dynamics and distinct functions of hypoxia in primary tumor growth and organotropic metastasis of breast cancer. *Cancer Res.* 2010;70:3905–14.
38. Achen MG, Stacker SA. Exit stage left: a tumor cell's journey from lymph node to beyond. *Trends Cancer.* 2018;4:519–22.
39. Lee CK, Jeong SH, Jang C, Bae H, Kim YH, Park I, et al. Tumor metastasis to lymph nodes requires YAP-dependent metabolic adaptation. *Science.* 2019;363:644–9.
40. Xiao BB, Chen QY, Sun XS, Li JB, Luo DH, Sun R, et al. *Low value of whole-body dual-modality [<sup>18</sup>F]Fluorodeoxyglucose Positron Emission Tomography/Computed Tomography in primary staging of stage I-II nasopharyngeal carcinoma: a nest case-control study.* *Eur Radiol.* 2021;31:5222–33.
41. Lowe VJ, Duan F, Subramaniam RM, Sicks JD, Romanoff J, Bartel T, et al. *Multicenter trial of [<sup>18</sup>F]Fluorodeoxyglucose Positron Emission Tomography/Computed Tomography staging of head and neck cancer and negative predictive value and surgical impact in the N0 neck: results from ACRIN 6685.* *J Clin Oncol.* 2019;37:1704–12.
42. Liu YP, Wen YH, Tang J, Wei Y, You R, Zhu XL, et al. Endoscopic surgery compared with intensity-modulated radiotherapy in resectable locally recurrent nasopharyngeal carcinoma: a multicentre, open-label, randomised, controlled, phase 3 trial. *Lancet Oncol.* 2021;22:381–90.
43. See A, Chu C, Kiong KL, Teo C, Tan HK, Wong EWY, et al. Surgical salvage of recurrent nasopharyngeal cancer-a multi-institutional review. *Oral Oncol.* 2021;122:105556.
44. Mao Y, Wang S, Lydiatt W, Shah JP, Colevas AD, Lee AWM, et al. Unambiguous advanced radiologic extranodal extension determined by MRI predicts worse outcomes in nasopharyngeal carcinoma: Potential improvement for future editions of N category systems. *Radiother Oncol.* 2021;157:114–21.
45. Rosenthal EL, Moore LS, Tipirneni K, de Boer E, Stevens TM, Hartman YE, et al. Sensitivity and specificity of cetuximab-IRDye800CW to identify regional metastatic disease in head and neck cancer. *Clin Cancer Res.* 2017;23:4744–52.
46. **Statements and Declarations.**

## Tables

**Table.1 CAIX expression of human NPC specimens in our study.**

CAIX staining	Primary	Local recurrence	Metastases	Total
<b>Strong</b>	18 (17.8%)	6 (30%)	6 (6.7%)	30 (14.2%)
<b>Moderate</b>	57 (56.4%)	12 (60%)	31 (34.4%)	100 (47.4%)
<b>Weak</b>	16 (15.8%)	2 (10%)	29 (32.2%)	47 (22.3%)
<b>Negative</b>	10 (10%)	0 (0%)	24 (26.7%)	34 (16.1%)

Note: we define CAIX scores as negative (CAIX = 0), weak (CAIX < 0.5), moderate ( $0.5 \leq \text{CAIX} < 1.6$ ) and strong (CAIX  $\geq 1.6$ ). NPC, nasopharyngeal carcinoma; CAIX, carbonic anhydrase.

**Table. 2 Diagnostic values for identifying malignant and benign lymph nodes.**

5-8F	Threshold values	Sensitivity	Specificity	Accuracy	PPV	NPV
<i>In vivo</i>	MFI= 5.825	81.3%	93.8%	89.8%	92.8%	83.3%
<i>Ex vivo</i>	MFI= 2.860	87.5%	93.8%	94.9%	93.3%	88.2%

Note: 5-8F, human NPC cell line; PPV, positive predictor value; NPV, negative predictor value.

## Figures

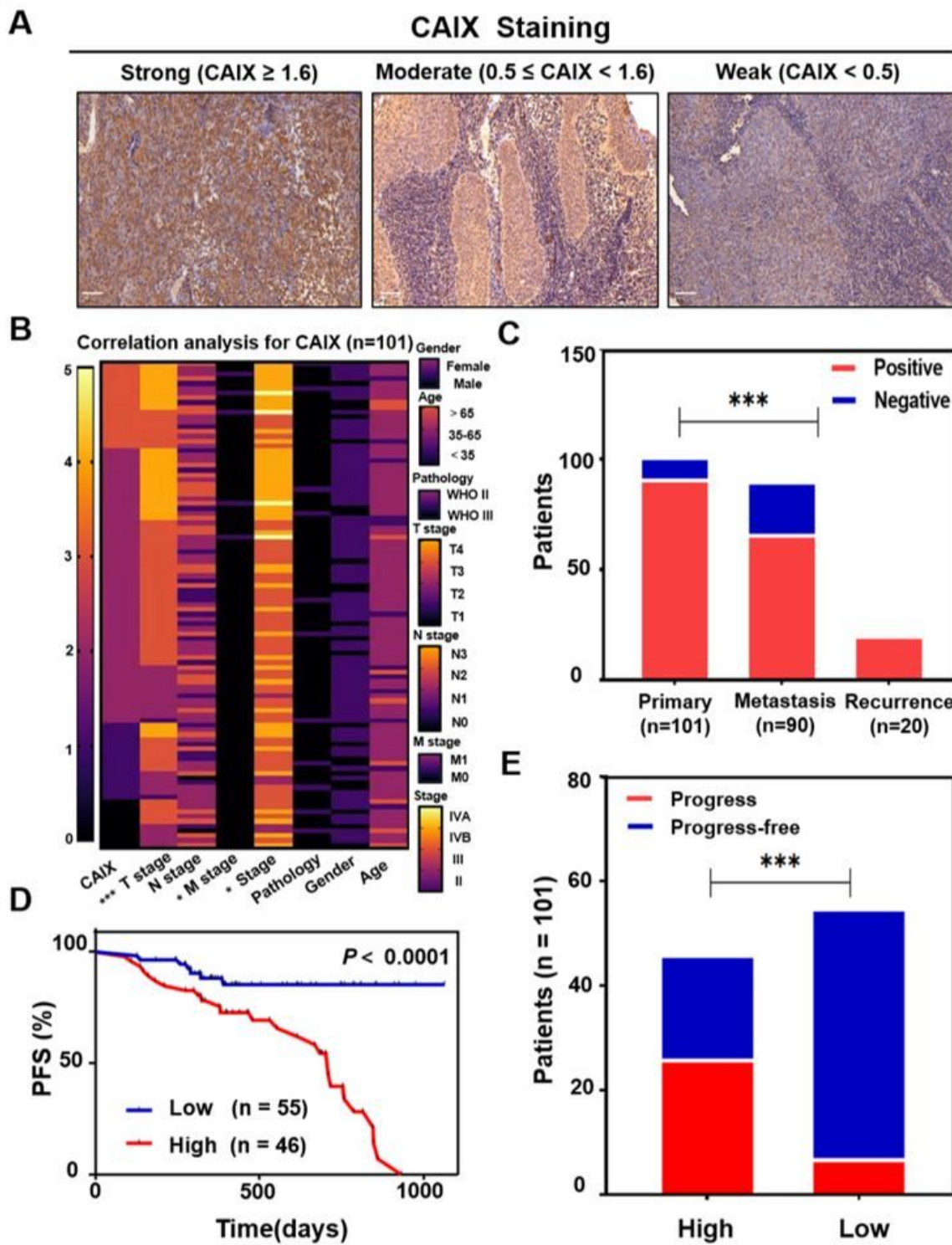


**Figure 1**

The clinical significance of CAIX expression in NPC patients. (A) The representative immunochemical images of CAIX expression. Scale bar = 50  $\mu\text{m}$ . (B) Heat map of the clinical annotations in correlation with CAIX expression in primary specimens (n = 101). Here we define four categories of CAIX expression: score = 3 (CAIX  $\geq 1.6$ ); score = 2 ( $0.5 \leq \text{CAIX} < 1.6$ ); score = 1 ( $0 < \text{CAIX} < 0.5$ ); score = 0 (CAIX = 0). Asterisks indicate significant associations with CAIX expression. (C) The frequency of CAIX expression in

primary tumors, metastasis, and local recurrence. (D) Kaplan-Meier curve for PFS in primary patients (n = 101) stratified by high score (CAIX  $\geq 1.16$ , red curve), and low score (CAIX < 1.16, blue curve). The tick marks on the curves indicate censoring during follow-up. (E) Two-sided Fisher's test in primary patients revealing CAIX as a risk factor for disease progression, with a risk ratio of 4.441 (95% CI: 2.217-9.308,  $p = 0.0008$ ). PFS, progression-free survival; CI, confidence interval. \* $p < 0.05$ ; \*\* $p < 0.01$ ; \*\*\* $p < 0.001$ .

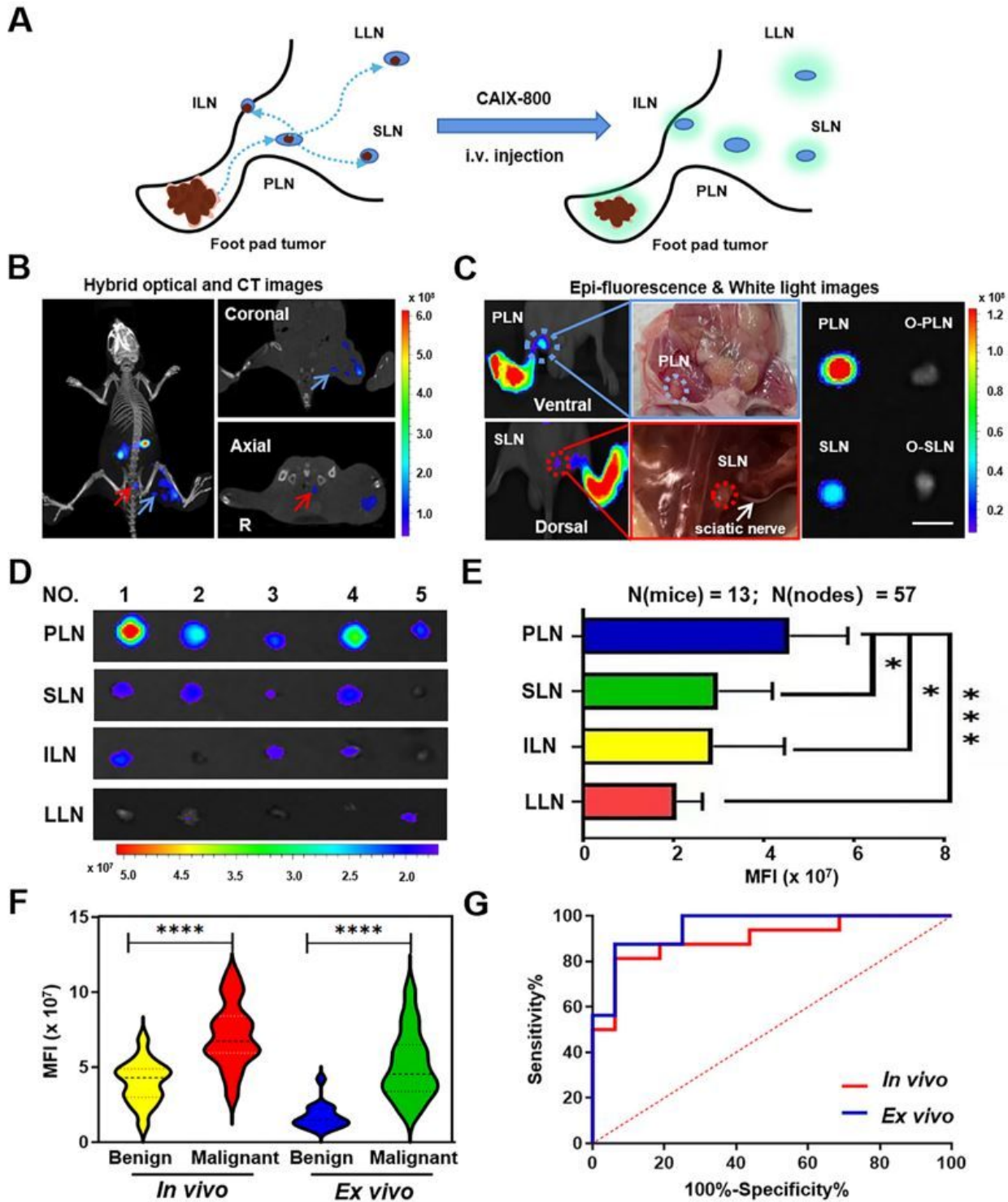
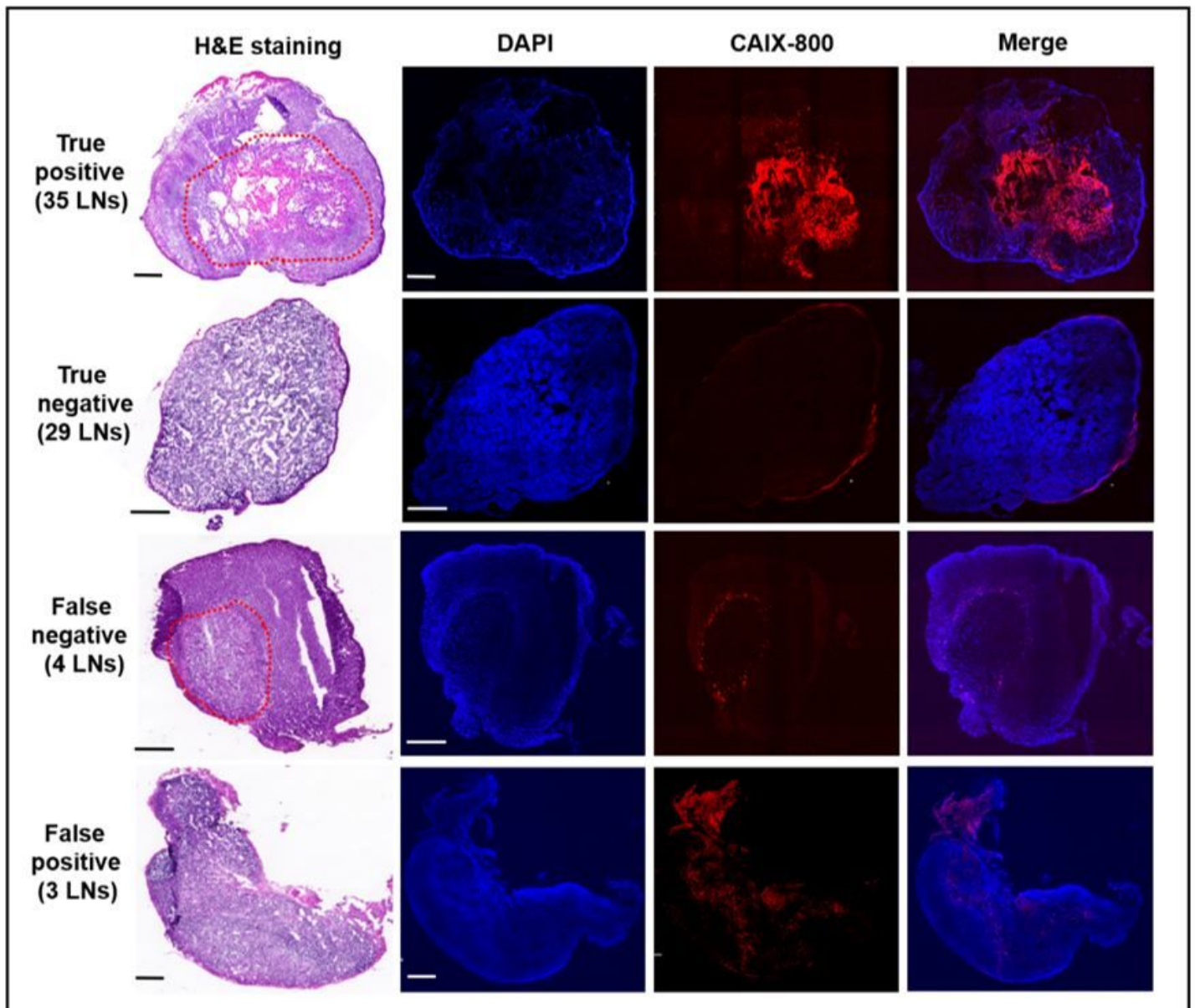


Figure 2

Mapping regional lymph node metastases (LNMs) using CAIX-800. (A) Schematic of CAIX-800 mapping LNMs. (B) Hybrid optical and micro-CT images of a mouse bearing right foot pad tumor and its draining LNs at 24 h post intravenous injection of CAIX-800. Blue arrow indicates the PLN on coronal CT, and red arrow represents the SLN on axial CT. (C) Corresponding 2D epi-fluorescence and white light images. O-PLN and O-SLN represent the opposite sites of PLN and SLN bearing none metastases. Scale bar = 3 mm. (D) *Ex vivo* fluorescent images of LNs resected from different regions. (E) Quantification of the MFI in regional LNs. (F) Quantitative analysis of fluorescent signal from malignant and benign LNs both *in vivo* and *ex vivo*. (G) ROC curve for discrimination between malignant and benign LNs. The AUCs were 0.89 *in vivo* (95% CI, 0.78-1.00) and 0.94 *ex vivo* (95% CI; 0.88-1.00). I.V., intravenous; LN, lymph node; PLN, popliteal lymph node; SLN, sciatic lymph node; ILN, inguinal lymph node; LLN, lumbar lymph node; MFI, mean fluorescence intensity; ROC, receiver operating characteristic; AUC, area under the curve. \* $p < 0.05$ ; \*\*\* $p < 0.001$ ; \*\*\*\* $p < 0.0001$ .



**Figure 3**

CAIX-800 distribution and correlation with H&E staining. A total of 71 LNs were collected from 14 mice bearing S18 foot pad xenografts. Representative images of CAIX-800 and H&E staining containing LNs bearing metastases (the first and the third rows), and uninvolved LNs (the second and the fourth rows). Dashed circles indicate the tumor region. H&E, hematoxylin and eosin. Scale bar = 200  $\mu$ m.

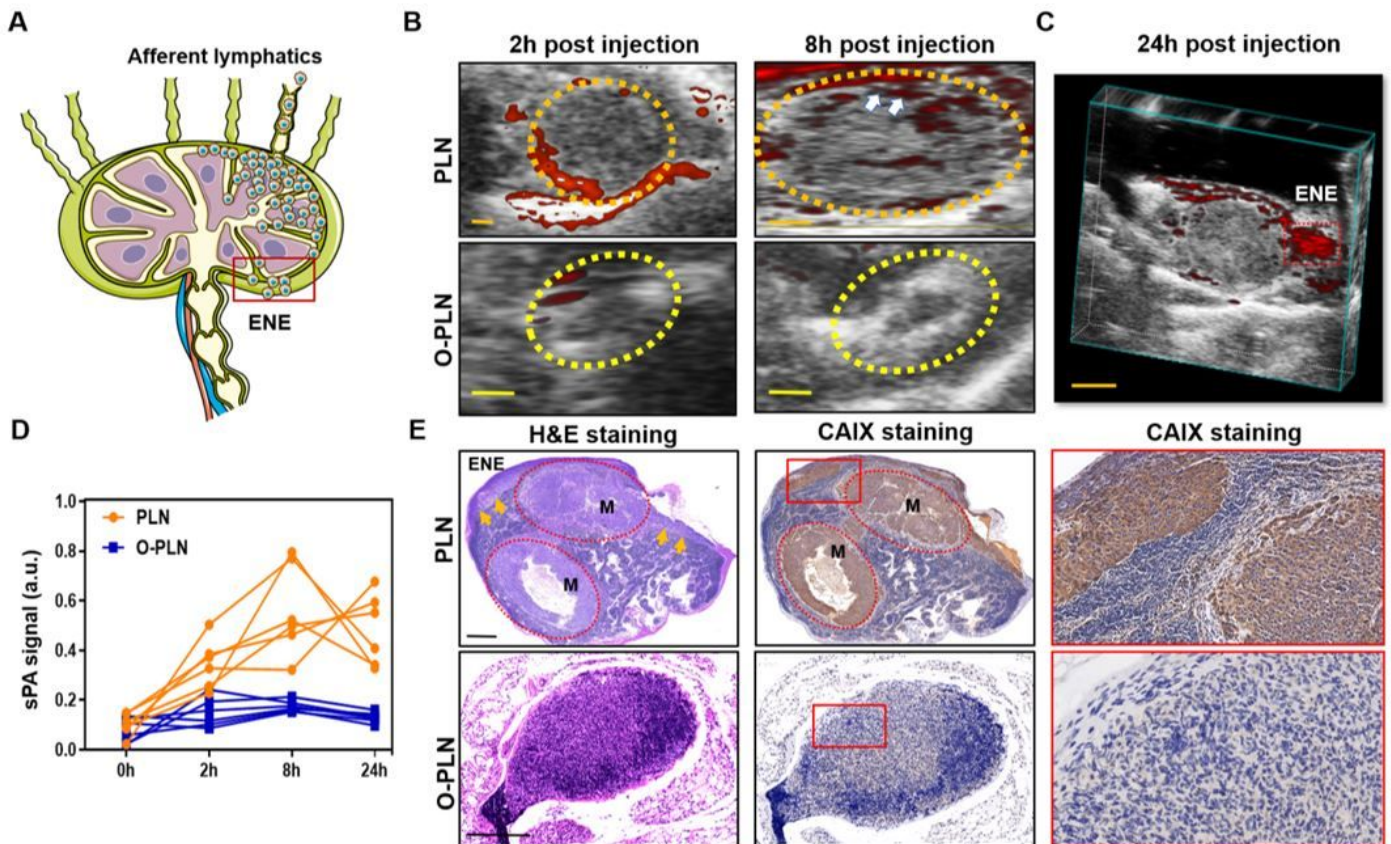


**Figure 4**

US-guided sPA imaging for identifying ENE. (A) Lymph node anatomy and a schematic of ENE showing cancer cells migration from afferent lymphatics to lymph node, then invasion into the perinodal space. (B) US-guided sPA images of benign (O-PLN, yellow dashed circle) and malignant (PLN, orange dashed circle) LNs. White arrows indicate sPA signal in subcapsular sinus. Scale bar = 500  $\mu$ m. (C) sPA signal remarkably distributing in the perinodal space at 24h post injection on 3D images. (D) Quantitative analysis of sPA signal within LNs at different time points post injection. (E) H&E and CAIX staining of nodal cross-sections. Orange arrows indicate the presence of ENE. The red circles show metastatic deposits, abbreviated as M. The rightmost panel represents the enlarged view at 20x magnification. Scale bar = 200  $\mu$ m. 3D, three dimensional; O-PLN, the opposite site of popliteal lymph node.

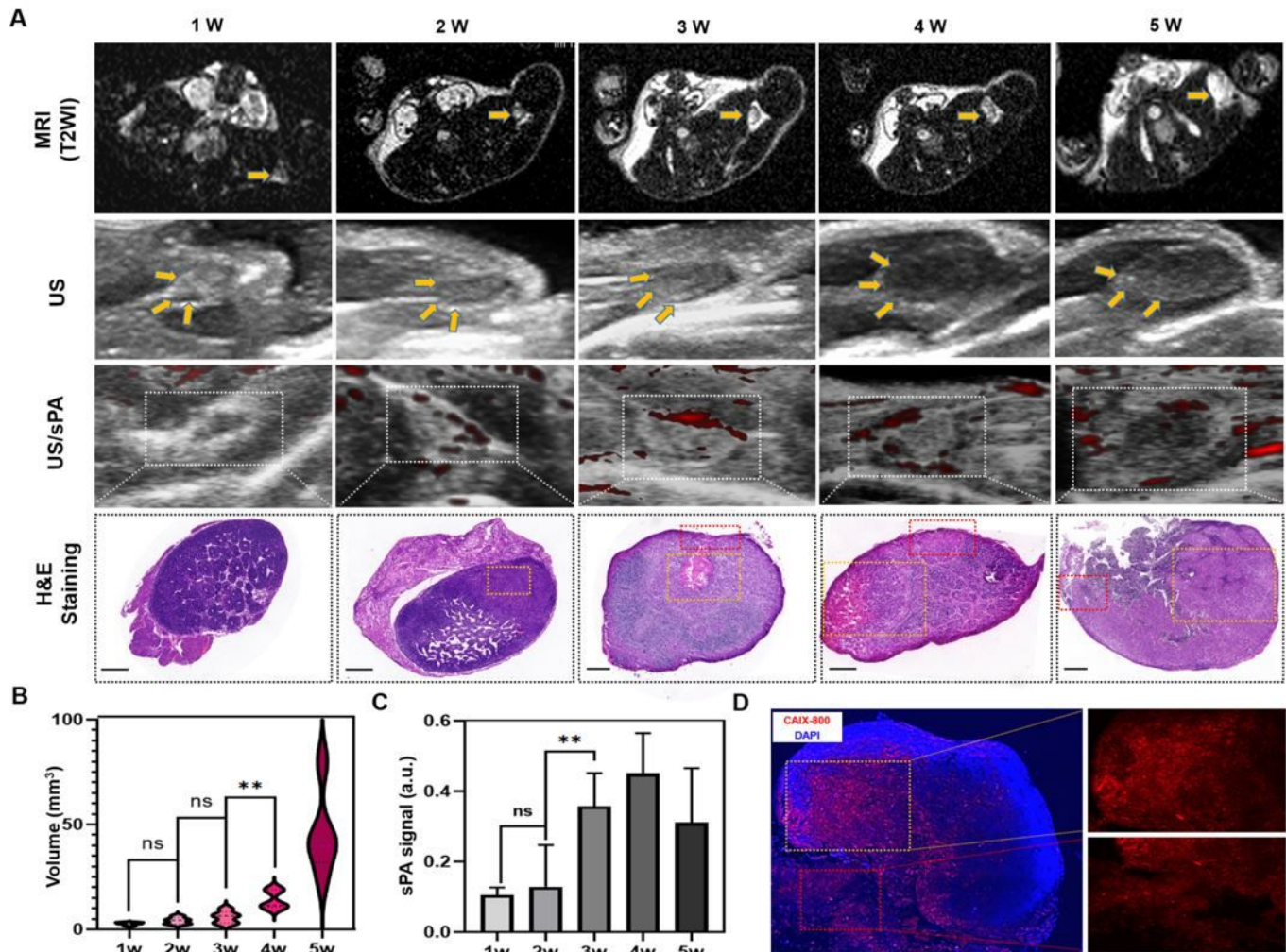


**Figure 5**

US-guided sPA imaging for detecting micro-metastases and tracking ENE. (A) MRI, US, US-guided sPA imaging, and H&E staining of the PLNs at different time points. Orange arrows and white dotted lines depict the PLNs. Red and orange rectangles indicate the ENE and metastatic deposits on microscopic images, respectively. Corresponding H&E confirms the imaging findings. (B) Nodal volumes recorded by sPA system. (C) Quantitative analysis of sPA signal within the PLNs. (D) Nodal cross-section at the 4th week. Section containing CAIX-800 (red) are counterstained with DAPI (blue) to visualize the nuclei. Orange rectangle indicates metastatic deposits. The probe labeled capsule (red rectangle) was peeled off *ex vivo*, explicating tumor infiltration. MRI, magnetic resonance imaging; DAPI, 4',6-diamidino-2-phenylindole. Scale bar = 200  $\mu$ m.

## Supplementary Files

This is a list of supplementary files associated with this preprint. Click to download.

- [GA.jpg](#)

- [Supplementarydata.pdf](#)
- [Video.1.mp4](#)